



HAL
open science

Pitting Corrosion of Type 316L Stainless Steel Elaborated by the Selective Laser Melting Method: Influence of Microstructure

V. Vignal, C. Voltz, S. Thiébaud, M. Demésy, O. Heintz, S. Guerraz

► **To cite this version:**

V. Vignal, C. Voltz, S. Thiébaud, M. Demésy, O. Heintz, et al.. Pitting Corrosion of Type 316L Stainless Steel Elaborated by the Selective Laser Melting Method: Influence of Microstructure. *Journal of Materials Engineering and Performance*, 2021, 30 (7), pp.5050-5058. 10.1007/s11665-021-05621-7 . hal-03410837

HAL Id: hal-03410837

<https://hal.science/hal-03410837v1>

Submitted on 1 Nov 2021

HAL is a multi-disciplinary open access archive for the deposit and dissemination of scientific research documents, whether they are published or not. The documents may come from teaching and research institutions in France or abroad, or from public or private research centers.

L'archive ouverte pluridisciplinaire **HAL**, est destinée au dépôt et à la diffusion de documents scientifiques de niveau recherche, publiés ou non, émanant des établissements d'enseignement et de recherche français ou étrangers, des laboratoires publics ou privés.



Pitting Corrosion of Type 316L Stainless Steel Elaborated by the Selective Laser Melting Method: Influence of Microstructure

V. Vignal, C. Voltz, S. Thiébaud, M. Demésy, O. Heintz, and S. Guerraz

Submitted: 17 December 2020 / Revised: 11 February 2021 / Accepted: 18 February 2021 / Published online: 17 March 2021

The microstructure of two sets of 316L alloys (SLM and wrought structure) is determined using SPECTROMAXx stationary metal analyzer, FE-SEM/EDS and XRD. The physical–chemical properties of the passive films are also investigated by means of XPS, Auger after sputtering and electrochemical impedance spectroscopy measurements. Differences and similarities between the two sets of alloys are then identified. The corrosion behavior of alloys is investigated in NaCl solution at the macro- and microscale (micro-capillary technique). It was found that the inclusion/particles cleanliness is the first-order parameter explaining differences between 316L(WS) and 316L(SLM). In the absence of particles (pure matrix), the two sets of alloys have the same corrosion behavior. Residual stresses, the average grain size, the PREN and the passive films properties are of second order.

Keywords austenite, passive film, pitting corrosion, selective laser melting

1. Introduction

Additive manufacturing (AM) is defined as the process of adding materials layer-by-layer to manufacture parts of three-dimensional work pieces (Ref 1, 2). Different AM technologies have been developed, such as direct metal laser sintering (DMLS), direct metal deposition (DMD), electron beam melting (EBM) or selective laser melting (SLM) (Ref 2). SLM enables the elaboration of metallic alloys and the fabrication of engineering components directly from metallic powder. Metal powder layers are fused by a laser source in a layer-by-layer manner into the required three-dimensional (3D) structure (Ref 2). The interaction of the metal powder and the laser beam raises the temperature to the melting point. It has been pointed out that the primary parameters that govern the microstructure of a 3D printed specimen are the laser power and the laser scan speed (Ref 3).

This invited article is part of a special topical focus in the *Journal of Materials Engineering and Performance* on Additive Manufacturing. The issue was organized by Dr. William Frazier, Pilgrim Consulting, LLC; Mr. Rick Russell, NASA; Dr. Yan Lu, NIST; Dr. Brandon D. Ribic, America Makes; and Caroline Vail, NSW Carderock.

V. Vignal and O. Heintz, ICB, UMR 6303 CNRS - Université de Bourgogne Franche Comté, BP 47870, 21078 Dijon, France; and Laboratoire Interactions Matériaux Procédés Environnements, LRC LIMPE n° DAM-VA-11-02, Dijon, France; C. Voltz, S. Thiébaud, and M. Demésy, Laboratoire Interactions Matériaux Procédés Environnements, LRC LIMPE n° DAM-VA-11-02, Dijon, France; and CEA, DAM, Centre d'études de Valduc, 21120 Is sur Tille, France; S. Guerraz, GMP ADDITIV, 74800 St Pierre en Faucigny, France. Contact e-mail: vincent.vignal@u-bourgogne.fr.

Due to the elaboration process conditions, alloys derived from SLM have specific microstructure when compared to alloys elaborated from conventional processing. A fine microstructure with columnar grains along the built direction is observed (Ref 4-7). The width of the elongated grains is $\sim 10 \mu\text{m}$. The microstructure is almost fully dense (low density of pores). In the case of 316L stainless steel, intercellular segregation of Mo, Cr and Si, resulting in creation of non-equilibrium eutectic ferrite is sometimes found (Ref 6). Transmission electron microscopy investigations (Ref 7) reveal the existence of a very fine dislocation cell structure in the as-built SLM sample with similarities to the deformation sub-structures obtained after severe plastic deformation.

The corrosion behavior of 316L derived from SLM may be significantly different from that of the alloy elaborated by classical methods (Ref 3, 8-19). Most of the papers show that 316L derived from SLM exhibits better corrosion resistance than 316L with wrought structure. However, the results can be relatively scattered. This scatter has never been discussed or interpreted. The main reason is that in all these studies, some information is often missing about the composition and microstructure of the substrate (content of minor elements such as carbon, sulfur and nitrogen, the presence of inclusions...) and the properties of the passive film (composition, thickness, density of dopants...).

According to the American Society Testing and Materials (ASTM), stainless steels are defined by grade composition ranges, and not by specifications. Therefore, the PREN of 316L is between 22.6 and 29.5 (first row in Table 1). In addition, large MnS inclusions can be found for sulfur contents greater than 200 ppm. Therefore, the chemical composition and microstructure must be determined accurately to ensure that studied alloys (SLM vs classical samples, for example) are comparable and to interpret correctly differences observed in the corrosion behavior.

In this paper, the microstructure of two 316L alloys (elaborated by SLM and from conventional processing) is investigated using SPECTROMAXx stationary metal analyzer,

Table 1 Chemical composition of alloys (wt.%) and values of the PREN (PREN = Cr + 3.3 × Mo + 16 × N)

	Cr	Ni	Mo	Mn	Si	C	N	P	S	Fe	PREN
ASTMA240/A240M	16-18	10-14	2-3	<2	<0.75	<300 ppm	<1000 ppm	<450 ppm	<300 ppm	Bal.	22.6-29.
316L(WS)	16.45	10.13	2.06	1.66	0.51	160 ppm	700 ppm	200 ppm	<5 ppm		24.4
316L powder	17.69	13.01	2.45	0.91	0.41	150 ppm	850 ppm	180 ppm	52 ppm		27.1
316L(SLM)	17.89	12.56	2.55	0.49	0.45	150 ppm	830 ppm	190 ppm	46 ppm		27.6
316L(SLM-1050)											
304L	18.17	10.13	0.2	1.13	0.4	180 ppm	730 ppm		44 ppm		20
316L	17.2	12.6	2.5	1.43	0.4	170 ppm	300 ppm		8 ppm		25.9
904L	19.55	24.2	4	1.41	0.2	210 ppm	740 ppm		2 ppm		34

surface observation methods (optical microscopy and field-emission scanning electron microscopy, FE-SEM) and x-ray diffraction (XRD, $\sin^2\psi$ method). The physical-chemical properties of the passive films are also determined by means of x-ray photoelectron spectroscopy (XPS), Auger electron spectroscopy (AES) after sputtering and electrochemical impedance spectroscopy (EIS) measurements (Mott-Schottky analysis). Differences and similarities between the two alloys are then identified. The corrosion behavior is then studied in 3.5% NaCl at 25 °C using potentiodynamic tests. Differences in the corrosion behavior are analyzed considering the composition and microstructure (PREN, average grain size, the presence of particles/inclusions) as well as the properties of the passive film.

2. Experimental Procedure

2.1 Materials and Surface Preparation

Two 316L stainless steel alloys were investigated, including an alloy with a wrought structure (noted 316L(WS)) and an alloy elaborated by SLM (316L(SLM)). The chemical composition of 316L(WS) is reported in Table 1. It was solution-annealed at 1050 °C for 15 min and quenched in water. To establish a relationship between the PREN and the pitting potential, three other alloys with a wrought structure were studied (noted 304L, 316L and 904L in Table 1).

The SLM alloy (noted 316L(SLM)) was elaborated by the use of an EOS M290 (EOS GmbH, Krailling, Germany) with an Yb-fiber laser (wavelength of 1070 nm and power of 400 W) having a laser diameter of 100 μm (corresponding to the hatch spacing). The input energy density was kept fixed at 100 J mm^{-3} . Experiments were conducted in an inert nitrogen-purged atmosphere. A cross-hatching strategy with a rotation angle of 60° between consecutive layers was selected. The chemical composition of the powder (average particle size of $32.9 \pm 11.3 \mu\text{m}$, error = standard deviation) is reported in Table 1. A heat treatment was then applied to 316L(SLM) in air. It consists in rising temperature up to 1050 °C in 150 min (420 °C/h) from room temperature, maintaining 1050 °C for 30 min and applying water quenching. This heat-treated alloy is noted 316L(SLM-1050). After heat treatment, a 1-mm thick layer was removed by grinding samples.

316L(WS), 316L(SLM) and 316L(SLM-1050) samples (height of 5 mm and diameter of 4 cm) were embedded in an epoxy resin. In the case of 316L(SLM) and 316L(SLM-1050), the surface studied is perpendicular to the build-up direction of

the additively manufactured workpieces (XY-plane). All samples were ground using emery papers (1200, 2400 and 4000 grits) and polished with diamond pastes (6, 3 and 1 μm). A specific vibratory polishing (VibroMet 2 vibratory polisher from Buehler) was then applied to remove the cold worked layer generated during the previous steps.

2.2 Surface Analysis and XRD Measurements

The chemical composition of native passive films was determined from XPS and AES measurements. A PHI Versaprobe 5000 apparatus with a monochromated Al K α 1 line (energy of 1486.7 eV, power of 50 W and x-ray spot diameter of 200 μm) was used for XPS analyses. The C1s peak from pollution (at 284.8 eV) was considered for the energy calibration. Spectra were treated with the CasaXPS software package.

AES measurements were carried out using a PHI 5000 Versaprobe instrument, with an electron beam diameter of 500 μm . Depth profiling was performed using 500 eV argon ions with a sputtering rate of 2 nm min^{-1} . This sputtering rate was measured on a pure SiO₂ thermal oxide. Analyzed peaks are O (510 eV), C (275 eV), Fe (600 eV), Ti (421 eV), Cr (531 eV), Ni (849 eV) and Mo (184 eV). Acquisitions in direct mode were derivated for the measurement of intensities. Data were treated with the Multipack software package.

Residual stresses were measured using the XRD technique and the $\sin^2\psi$ method (Ref 20). A D8 Discovery Bruker four-circle diffractometer equipped with a large area detector (GADDS) was used. The x-rays were generated by a Co tube ($\lambda_{\text{Co}} = 0.179 \text{ nm}$) and the surface area analyzed was 3.1 mm^2 .

2.3 Electrochemical Measurements

All electrochemical experiments were carried out in 3.5 wt.% NaCl at 25 °C using a PGSTAT128 AUTOLAB potentiostat/galvanostat. Experiments were performed at the global scale using a classical three-electrode cell. Potentials were measured vs. saturated calomel electrode (SCE) and the counter electrode was made of platinum grid (5 × 5 cm^2). Polarization curves were plotted from −400 mV vs. SCE up to 1 V at a potential scan rate of 1 mV s^{-1} .

Mott-Schottky analyses were performed to investigate the semiconducting properties of native passive films. Electrochemical impedance spectroscopy (EIS) measurements were performed at 1.5 kHz. The Mott-Schottky plots were obtained by sweeping the potential range in the anodic direction, from −1000 to +1000 mV SCE. Potentials were applied by successive steps of 50 mV, with an amplitude sinusoidal voltage perturbation of 20 mV. Capacitance values were

calculated from the relation $C = (-2\pi f Z_{im})^{-1}$, where f is the frequency and Z_{im} is the imaginary part of the impedance.

3. Results and Discussion

3.1 Microstructures

316L(WS), 316L(SLM) and 316L(SLM-1050) have comparable carbon content (150-160 ppm in Table 1) and very low sulfur level (< 50 ppm in Table 1). The pitting resistance equivalent number (PREN) of 316L(SLM) and 316L(SLM-1050) is significantly greater than that of 316L(WS), Table 1. The difference (of about 3) must be taken into account when interpreting the corrosion results.

Figure 1(a), (b), (c) and (d) shows the microstructure of the three samples after etching (in 50%vol. HCl at 2 V for 10 s). Equiaxed grains are observed in 316L(WS), Figure 1(a). Annealing twins are also present in some grains. Both the hatching pattern and fine grains are visible in 316L(SLM), Fig. 1(b). After heat treatment, the hatching pattern is no longer visible, and only coarse grains are found, Fig. 1(c). The average grain size was determined using the circular intercept method according to ASTM E112. The average grain size is 53.4, 15.9 and 31.8 μm for 316L(WS), 316L(SLM) and 316L(SLM-1050), respectively. These results show that 316L(SLM) has the finest microstructure.

316L(WS) contains mixed oxide microparticles having a diameter between 1 and 5 μm (image insert in Fig. 1a). Al, Mg, Mn, Si, Ti and Ca are constituent elements of these microparticles. For example, energy dispersive spectroscopy (EDS) analysis of the microparticle in Fig. 1(a) yields (at.%) 63.5% O,

10.8% Si, 10.2% Al, 8.5% Ca, 3.2% Ti, 1.6% Mg and 0.9% Mn. This analysis was performed using JEOL JSM-7600F FE-SEM. It was already shown (Ref 21, 22) that microparticles containing CaO are precursor sites for pitting corrosion in stainless steels. By contrast, no MnS inclusions were found. In 316L(SLM) and 316L(SLM-1050), no mixed oxide microparticles, no MnS inclusions and no pores were found. The two samples contain spherical silicate nanoparticles (diameter $\ll 1 \mu\text{m}$, Fig. 1d) composed mostly of O (51.9 ± 4.1 at.%), Si (16.1 ± 1.1 at.%), Cr (13.2 ± 2.8 at.%) and Mn (9.1 ± 1.1 at.%). Therefore, differences observed between samples in the average grain size and in the nature of particles must be taken into account when interpreting the corrosion results.

Residual stresses were measured using the $\sin^2\psi$ method (Ref 20). A linear relationship was systematically found between the variation of the Bragg's angle, $\Delta 2\theta$, and $\sin^2\psi$, Fig. 2(a) and (b). The same slope was found for the three samples, corresponding to residual stress values of -66 ± 24 and -24 ± 14 MPa in the radial and orthoradial directions, respectively. As expected (vibratory polishing), residual stresses are very low. The same level of residual stresses was obtained in the three samples. Therefore, differences observed in the corrosion behavior cannot be interpreted considering this parameter.

3.2 Properties of Passive Films

There is a limited number of papers about the physical-chemical properties of passive films formed on 316L alloys elaborated by SLM. AES analyses (Ref 23) do not show significant differences in the chemical composition and thickness of the passive films formed in alkaline solution under

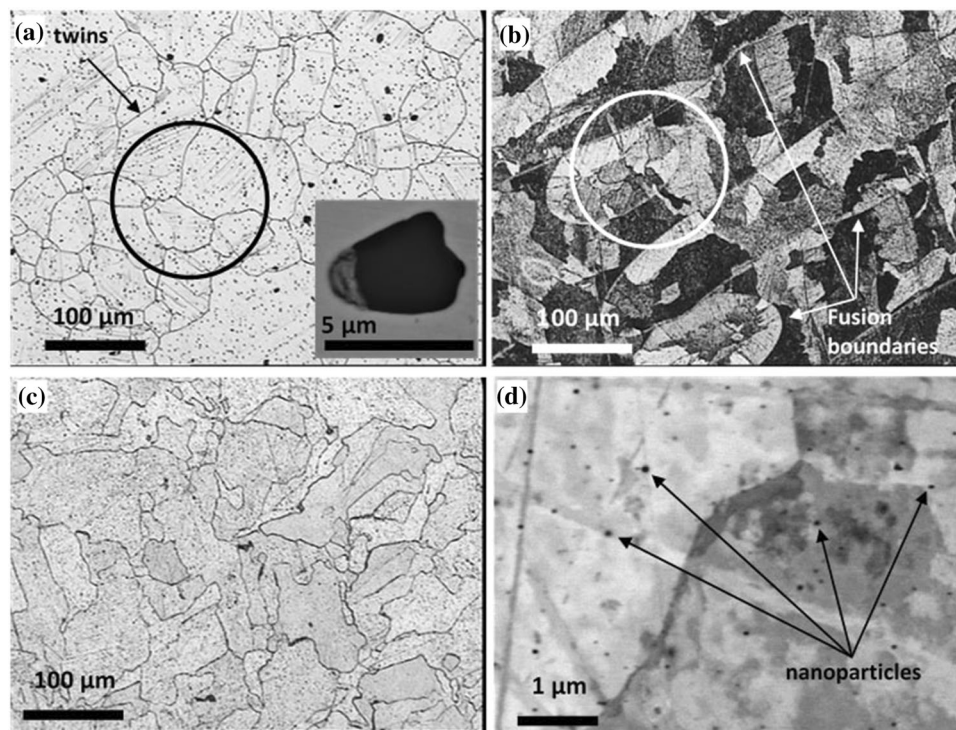


Fig. 1 Optical images after etching in 50% HCl at 2 V for 10 seconds of (a) 316L(WS) (insert image: mixed oxide microparticle), (b) 316L(SLM) and (c) 316L(SLM-1050). (d) FE-SEM image after surface preparation of silicate nanoparticles in 316L(SLM). The circle in (a) represents the diameter of the capillary used for local electrochemical measurements

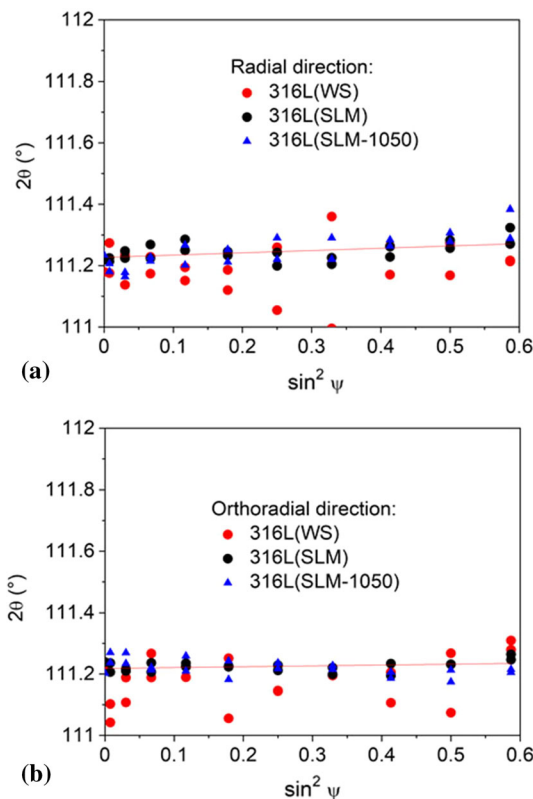


Fig. 2 2θ vs. $\sin^2 \psi$ plots after surface preparation: (a) radial and (b) orthoradial directions

potentiostatic conditions for 12 hours. By contrast, XPS and TEM investigations (Ref 24) reveal some differences in the structure of these passive films. It was proposed that these differences might lead to a more protective passive film on the sample elaborated by SLM. In addition, there are no data about the physical–chemical properties of native passive films.

XPS experiments were carried out to characterize the composition of the three native passive films. Mo3d spectra were decomposed as proposed in (Ref 25), Figure 3(a) and (b). Mo^{6+} and Mo^{4+} species were found, and no differences were observed between the three samples. C1s, O1s, Fe2p and Cr2p spectra were decomposed into classical contributions according to (Ref 26, 27). A peak was found at 283 eV in the C1s spectrum of 316L(SLM-1050) which was attributed to the presence of carbides, Fig. 3(c). This study is an example of the formation of carbides due to the heat treatment conditions described in section 2.1. Depending on the heat treatment strategy (Ref 17, 18, 28, 29), precipitation can occur and/or the distribution of dislocations and alloying elements, the grain size and orientation and the nature of grain boundaries can be modified. The ratio $\text{O}^{2-} / \text{OH}^-$ in the native passive films was calculated from the O1s spectra, Fig. 3(d). Numerical values are reported in Table 2. The highest value was found for 316L(SLM-1050), of about 2 (between 1.3 and 1.4 for 316L(W.S) and 316L(SLM)). This ratio plays also an important role in pitting corrosion (Ref 30). Indeed, passivity of metallic alloys is usually attributed to the presence of oxides at the specimen surface rather than hydroxides. Therefore, the native passive film formed on 316L(SLM-1050) is slightly richer in oxides than the two others.

Regarding alloying elements, the native passive film on 316L(SLM) contains the lowest amount of Fe-based species (oxides and hydroxides), Fig. 4(a). On the other hands, the native passive films on 316L(SLM) and 316L(SLM-1050) contain the lowest amount of Cr-based species (oxides and hydroxides), Fig. 4(b). The ratio Cr / Fe in the native passive films is more relevant to interpret the corrosion resistance of alloys rather than the Cr and Fe contents. It was already shown that the greater the ratio Cr/Fe in the passive film, the higher the corrosion resistance of the alloy (Ref 31, 32). The values of Cr / Fe were calculated from AES profiles, Fig. 5 and Table 2. The same value of Cr/Fe was found in the three cases (values around 0.5). This ratio is less than unity, indicating that all native passive films are richer in iron-containing species than in chromium-containing ones.

The thickness of the native passive films on 316L(W.S) and 316L(SLM) is around 1 nm (Fig. 5a and b) and Table 2). The thickness is regarded as the sputtering distance at which oxygen content reduces to half relative to that at the surface. The depth profile of oxygen on 316L(SLM-1050) is different from that on the two other samples, Fig. 5(c). This could mean that the passive film is thicker or that the thickness is comparable but the sputtering rate is slower (passive film enriched with oxides which are more difficult to sputter than hydroxides).

Figure 6 shows the Mott–Schottky plots of the native passive films. All plots reveal two linear parts corresponding to Mott–Schottky-type behaviors (Ref 33). For applied potentials less than -600 mV vs. SCE, a p-type semiconducting behavior which is attributed to the predominant formation of chromium oxide in the inner part of passive films is found. In the anodic region (potentials greater than -600 mV vs. SCE), the capacitance represents the behavior of a n-type semiconductor characterizing the outer hydroxide layer of native passive films. The density of acceptors and donors was calculated from the negative and positive slopes, respectively (Eq 1).

$$N = \frac{2}{\epsilon \cdot \epsilon_0 \cdot q \cdot p} \quad (\text{Eq 1})$$

where ϵ is the relative permittivity ($\epsilon = 15.6$ (Ref 23)), ϵ_0 is the vacuum permittivity ($8.854 \times 10^{-12} \text{ F m}^{-1}$), q is the electron charge ($1.602 \times 10^{-19} \text{ C}$) and p is the slope ($\text{F}^{-2} \text{ m}^4 \text{ V}^{-1}$). Numerical values of the density of acceptors (N_a) and donors (N_d) are reported in Table 2. Results obtained on 316L(W.S) and 316L(SLM-1050) are similar. The native passive film formed on 316L(SLM) contains the highest density of dopants (both acceptors and donors). This sample has the finest microstructure and therefore the highest density of grain boundaries. However, differences between the three samples are very small. The density of dopants in 316L(SLM) is 1.4–1.8 times higher than in the other samples.

AES and XPS results show that the native passive films have the same chemical composition. The native passive film on SLM(SLM-1050) is slightly thicker than on the two other samples. In addition, electrochemical measurements reveal that differences in the density of dopants between the three samples are small.

3.3 Corrosion Behavior of Samples in 3.5wt.% NaCl

Figure 7(a) shows the polarization curves of 316L(W.S), 316L(SLM) and 316L(SLM-1050) in 3.5% NaCl (25 °C) at the global scale. It can be observed that the method of elaboration

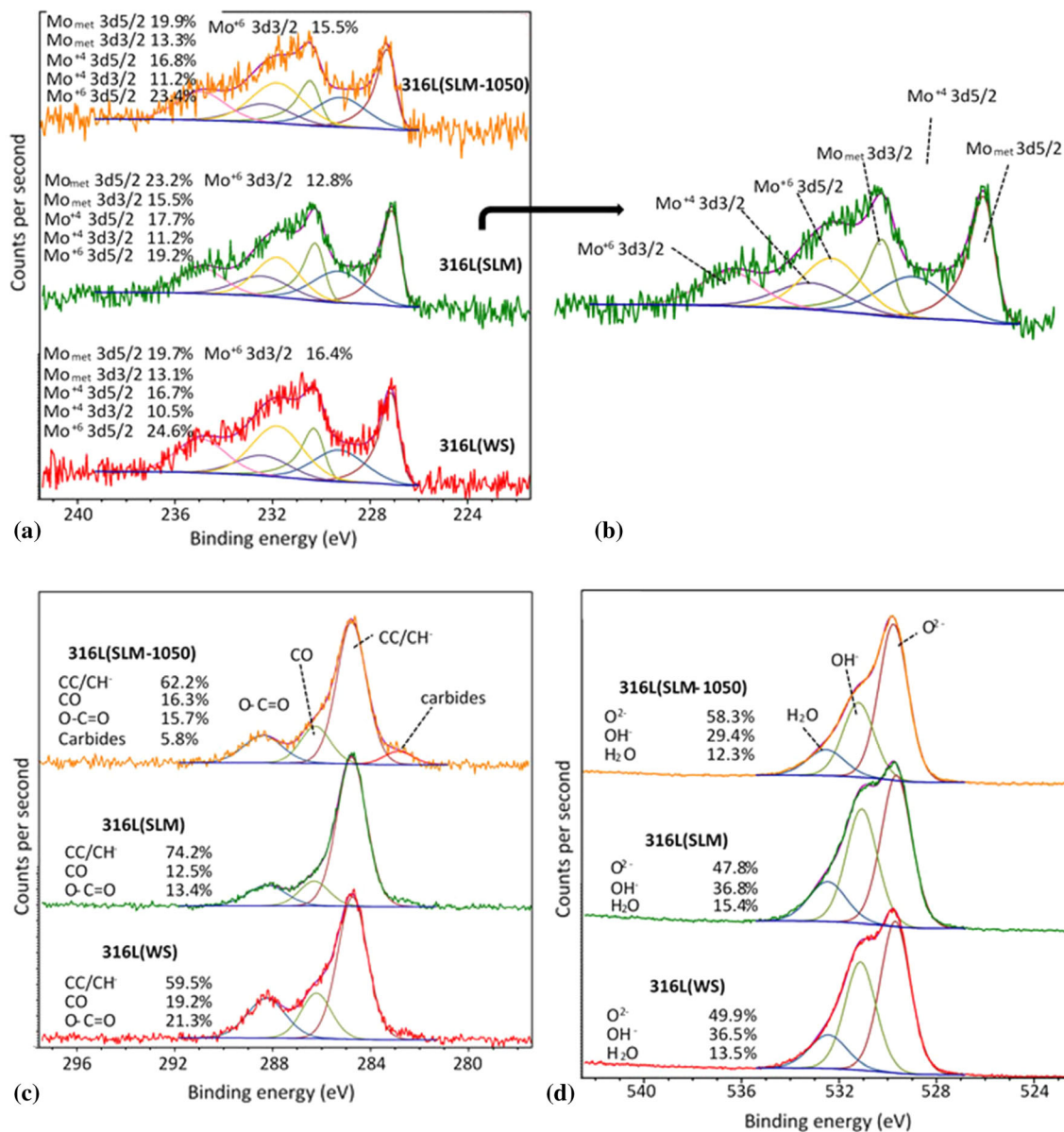
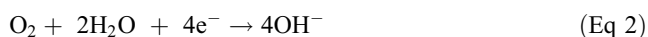


Fig. 3 XPS spectra of 316L(WS), 316L(SLM) and 316L(SLM-1050) after surface preparation: (a-b) Mo3d levels, (c) C1s and (d) O1s

Table 2 Quantitative data derived from (*) Auger, (**) XPS and (***) EIS measurements after surface preparation

	Thickness* (nm)	Cr/Fe*	O ²⁻ /OH ⁻ **	Na** (× 10 ¹² cm ⁻³)	Nd*** (× 10 ¹² cm ⁻³)
316L(WS)	1	0.5	1.4	1.2	1
316L(SLM)	1	0.5	1.3	1.7	1.8
316L(SLM-1050)	2.5	0.5	2	1.3	1.3

and the heat treatment have no influence on the current density in the cathodic branch. The main cathodic reaction is the oxygen reduction reaction (ORR, reaction 2).



316L(SLM) exhibits passive behavior. No stable and metastable pitting is observed in the anodic domain, Fig. 7(a). By contrast, stable pitting is observed in 316L(WS) and 316L(SLM-1050) at an applied potential of 0.5 and 0.4 V

vs. SCE, respectively. To confirm that stable pitting occurs in 316L(SLM-1050), the potential of 1 V vs SCE was maintained at the end of the polarization curve for a sufficiently long time. The current density increases continuously to values greater than 1 mA/cm² (and the pits were found to be larger than right after the polarization curve). The current peaks observed in the passive range of the polarization curve of 316L(SLM-1050) correspond to potential transients (metastable pitting) rather than oxidation peaks. Indeed, two polarization curves were

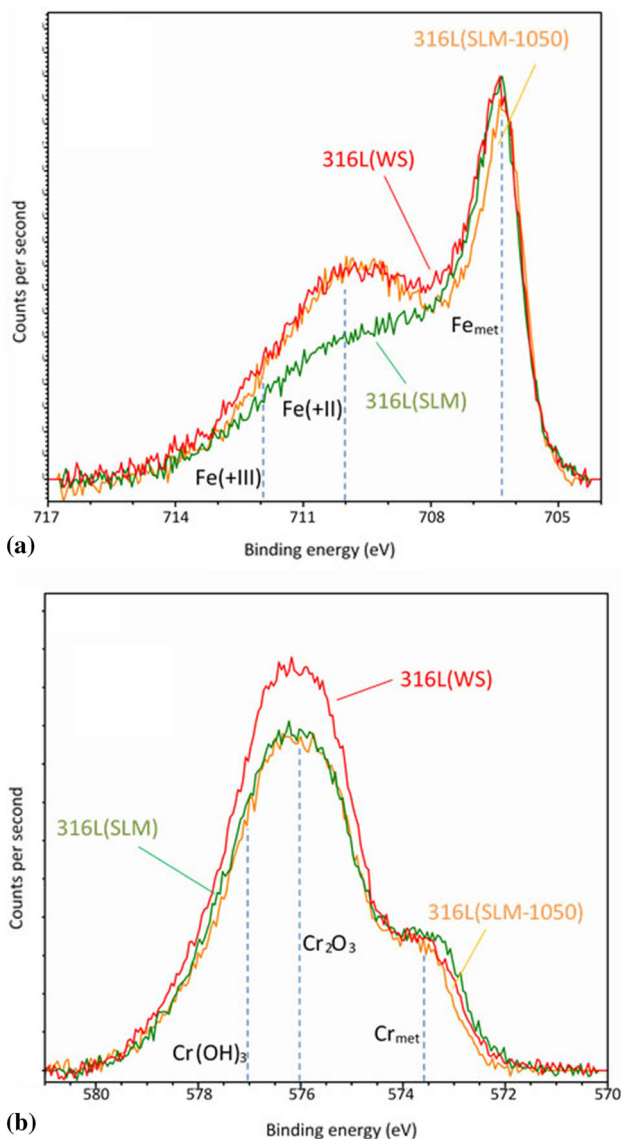


Fig. 4 XPS spectra of 316L(WS), 316L(SLM) and 316L(SLM-1050) after surface preparation: (a) Fe2p, (b) Cr2p levels

plotted, and these peaks were not systematically observed. Figure 8 shows pits observed in 316L(WS) and 316L(SLM-1050) after polarization curves. They were significantly larger in the wrought structure than in the 316L(SLM-1050). The influence of the microstructure and elaboration method on the pit propagation stage is an important scientific issue that we will be studied in the future.

Considering the results presented in the previous sections, two different assumptions may explain the excellent corrosion resistance of 316L(SLM) with respect to 316L(WS): the greatest value of the PREN (chemical composition of the matrix) and/or the absence of mixed oxide microparticles.

Figure 7(b) shows the evolution of the pitting potential vs the PREN value. To determine this evolution, global polarization curves of additional austenitic alloys with wrought structure were plotted in 3.5% NaCl at 25 °C, after vibratory polishing. Among these austenitic alloys, there is type 304L stainless steel (PREN = 20), a second type 316L (PREN = 25) and a super-austenitic 904L stainless steel (PREN = 35),

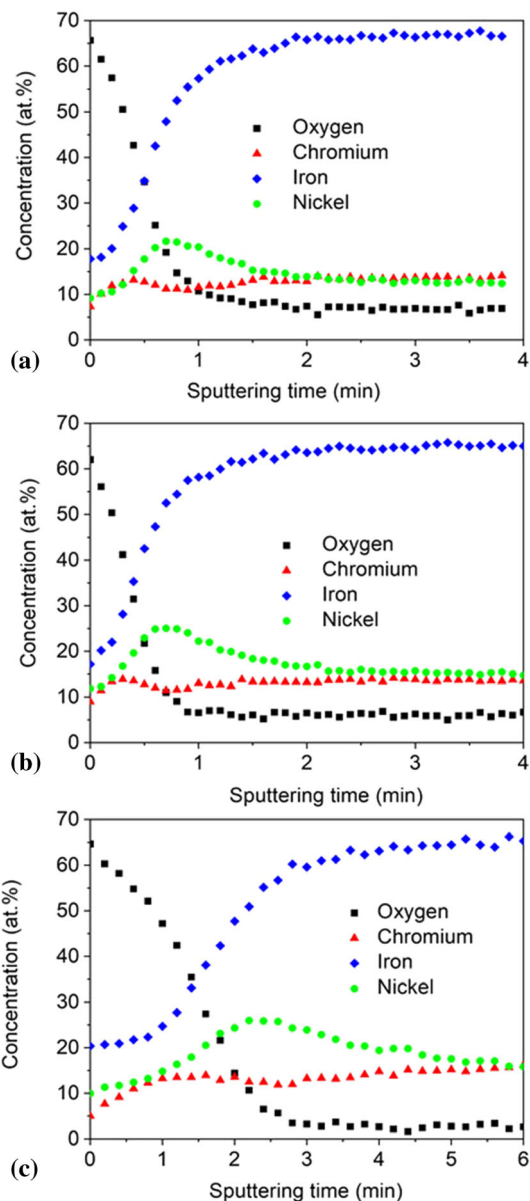


Fig. 5 Auger depth profiles of oxygen and alloying elements (Fe, Cr, Ni) for: (a) 316L(WS), (b) 316L(SLM) and (c) 316L(SLM-1050) after surface preparation

Table 1. All these alloys have very low carbon (< 150 ppm) and sulfur (< 50 ppm) contents. They contain mixed oxide microparticles (as that shown in Fig. 1a). A linear relationship was found between the pitting potential and the PREN value (dotted line in Fig. 7b). According to this relationship, 316L(SLM) which have a PREN of 27.6 should exhibit stable pitting at around 630 mV vs SCE. This is not in good agreement with the results shown in Fig. 7a (no stable pitting in 316L(SLM)). This suggests that the PREN is not the first-order parameter controlling pitting corrosion of the studied alloys.

Local polarization curves were then plotted in sites of 316L(WS) containing the matrix without mixed oxide microparticles, Fig. 9. The measurements were performed under the same experimental conditions than at the global scale (3.5% NaCl at 25 °C, 1 mV/s) using the electrochemical microcell technique (Ref 33-36) and capillaries with a diameter

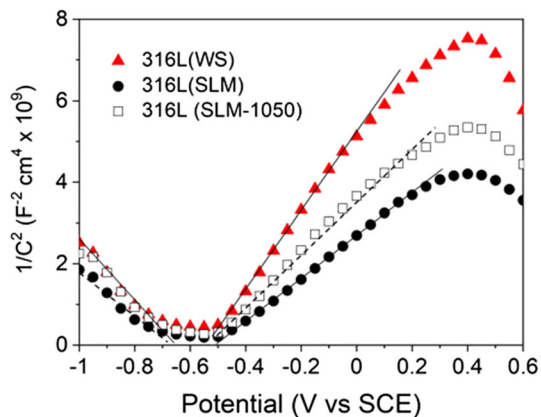


Fig. 6 Mott-Schottky plots for the native passive films after surface preparation

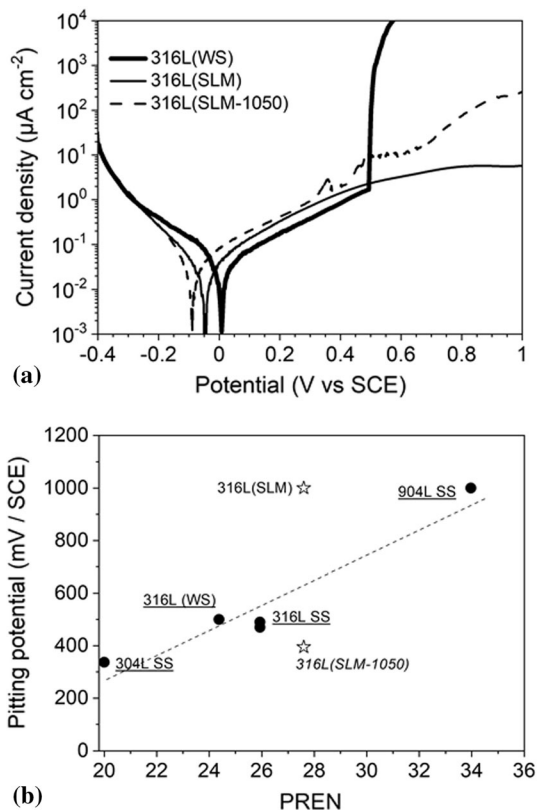


Fig. 7 (a) Global polarization curves (3.5% NaCl à 25°C, 1 mV s^{-1}) of the different samples after surface preparation. (b) Relationship between pitting potential derived from global polarization curves and PREN for different austenitic alloys

of $154 \mu\text{m}$. As shown in Fig. 1(a), several grains and grain boundaries are present within the investigated surface. A large number of local polarization curves (about 10 curves) were plotted in different sites to ensure that all potential weak points (except oxide microparticles) are considered. As obtained results were very reproducible, only two typical curves are shown. The matrix of 316L(WS) without mixed oxide microparticles exhibits passive behavior, Fig. 9. No stable and metastable pitting is observed in the anodic domain. Although the matrices of 316L(WS) and 316L(SLM) are

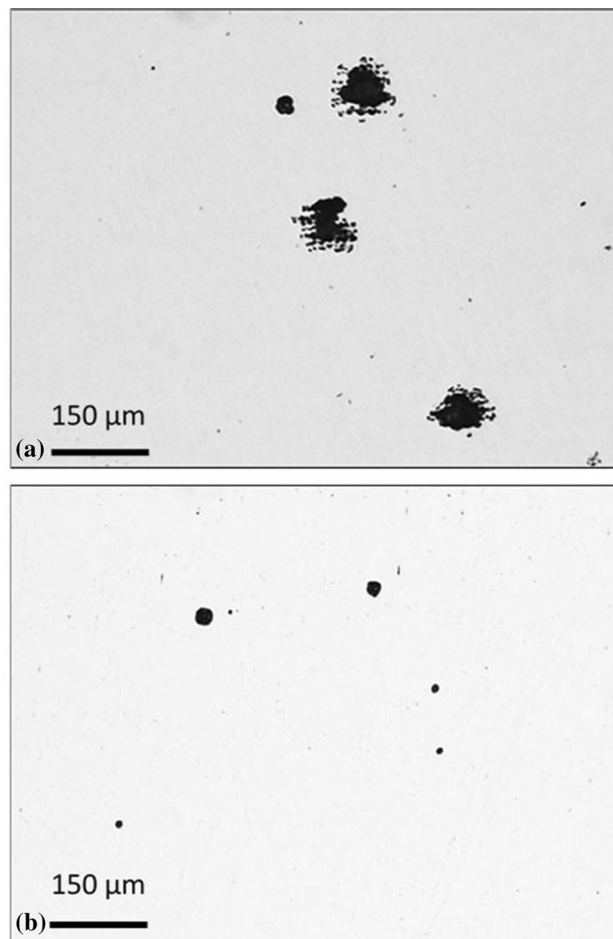


Fig. 8 Optical micrographs of the surface after the polarization curve: (a) 316L(WS) and (b) 316L(SLM-1050)

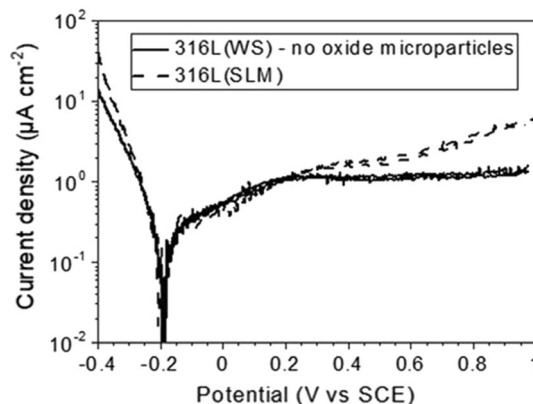


Fig. 9 Local polarization curves (3.5% NaCl à 25°C, 1 mV s^{-1} , capillary diameter of $154 \mu\text{m}$) after surface preparation of 316L(WS) and 316L(SLM)

different in terms of average grain size and PREN, they have similar corrosion behavior in 3.5% NaCl at 25 °C (passive behavior, no pitting). These results show that mixed oxide microparticles present in the alloy elaborated by classical processing are precursor sites for pitting.

Local polarization curves were plotted in sites of 316L(SLM) under the same experimental conditions, Fig. 9.

Several grains and grain boundaries are again present within the investigated surface (Fig. 1b). As it was already found at the macroscale, no pitting potential can be defined from local polarization curves. 316L(SLM) has passive behavior in 3.5% NaCl. The current density in the passive range is slightly greater than that measured on 316L(WS). This is mainly due to the fact that the native passive film formed on 316L(SLM) contains a higher density of dopants than the passive film on 316L(WS), Fig 6.

The pitting potential of 316L(SLM-1050) was found to be lower than the value expected from the linear relationship between the pitting potential and the PREN, Fig. 7(b). The presence of carbides revealed by XPS (section 3.2) greatly reduces the corrosion resistance of 316L(SLM-1050) compared to that expected with its PREN value. Other studies (Ref 18, 37) have revealed that chromium carbides are precursor sites in 316L stainless steel. The positive influence of the ratio O^{2-}/OH^- in the native passive film (section 3.2) is then counter-balanced by the negative role of carbides. The corrosion resistance of 316L elaborated by SLM can increase after certain heat treatment, while others may reduce it (Ref 17, 18, 28, 29). It depends on modifications of the microstructure and physical-chemical properties of the passive film formed after aging in aqueous solutions.

4. Conclusions

The corrosion behavior of 316L(WS), 316L(SLM) and 316L(SLM-1050) was analyzed considering their microstructure, residual stresses and the physical-chemical properties of native passive films. Obtained results show that the PREN and the average grain size are not the first-order parameters controlling pitting corrosion of the studied alloys. Precursor sites in 316L(WS) are mixed oxide particles (with Ca, Al, Mg, Ti...). In the absence of mixed oxide particles, 316L(WS) has the same corrosion behavior than 316L(SLM) in 3.5% NaCl at 25 °C (passive behavior with no pitting potential). Therefore, the inclusion/particles cleanliness is the first-order parameter explaining differences between 316L(WS) and 316L(SLM). After heat treatment at 1050 °C for 6 hours, carbides are precursor sites in 316L(SLM-1050).

Open Access

This article is licensed under a Creative Commons Attribution 4.0 International License, which permits use, sharing, adaptation, distribution and reproduction in any medium or format, as long as you give appropriate credit to the original author(s) and the source, provide a link to the Creative Commons licence, and indicate if changes were made. The images or other third party material in this article are included in the article's Creative Commons licence, unless indicated otherwise in a credit line to the material. If material is not included in the article's Creative Commons licence and your intended use is not permitted by statutory regulation or exceeds the permitted use, you will need to obtain permission directly from the copyright holder. To view a copy of this licence, visit <http://creativecommons.org/licenses/by/4.0/>.

References

1. Y. Oh, C. Zhou, and S. Behdad, Part Decomposition and Assembly-Based (Re) Design for Additive Manufacturing: A Review, *Addit. Manuf.*, 2018, **22**, p 230–242
2. G.H. Loh, E. Pei, D. Harrison, and M.D. Monzón, An Overview of Functionally Graded Additive Manufacturing, *Addit. Manuf.*, 2018, **23**, p 34–44
3. G. Sander, S. Thomas, V. Cruz, M. Jurg, N. Birbilis, X. Gao, M. Brameld, and C.R. Hutchinson, On the Corrosion and Metastable Pitting Characteristics of 316L Stainless Steel Produced by Selective Laser Melting, *J. Electrochem. Soc.*, 2017, **164**, p C250–C257
4. C. Wang, X. Tan, E. Liu, and S.B. Tor, Process Parameter Optimization and Mechanical Properties for Additively Manufactured Stainless Steel 316L Parts by Selective Electron Beam Melting, *Mater. Des.*, 2018, **147**, p 157–166
5. F. Rosa, S. Manzoni, and R. Casati, Damping Behavior of 316L Lattice Structures Produced by Selective Laser Melting, *Mater. Des.*, 2018, **160**, p 1010–1018
6. T. Kurzynowski, K. Gruber, W. Stopyra, B. Kuźnicka, and E. Chlebus, Correlation Between Process Parameters, Microstructure and Properties of 316 L Stainless Steel Processed by Selective Laser Melting, *Mater. Sci. Eng. A*, 2018, **718**, p 64–73
7. S. Gorsse, C. Hutchinson, M. Gouné, and R. Banerjee, Additive Manufacturing of Metals: A Brief Review of the Characteristic Microstructures and Properties of Steels, Ti-6Al-4V and High-Entropy Alloys, *Sci. Technol. Adv. Mater.*, 2017, **18**, p 584–610
8. S.M. Yusuf, M. Nie, Y. Chen, S. Yang, and N. Gao, Microstructure and Corrosion Performance of 316L Stainless Steel Fabricated by Selective Laser Melting and Processed through High-Pressure Torsion, *J. Alloys Compd.*, 2018, **763**, p 360–375
9. Q. Chao, V. Cruz, S. Thomas, N. Birbilis, P. Collins, A. Taylor, P.D. Hodgson, and D. Fabijanic, On the Enhanced Corrosion Resistance of a Selective Laser Melted Austenitic Stainless Steel, *Scripta Mater.*, 2017, **141**, p 94–98
10. A. Kurian and P.M. Siva, A comparison of corrosion resistance of stainless steel fabricated with selective laser melting and conventional processing, *Int. J. Chemtech Res.*, 2014–2015, **7**, p 2632–2635
11. Y. Zhang, F. Liu, J. Chen, and Y. Yuan, Effects of Surface Quality on Corrosion Resistance of 316L Stainless Steel Parts Manufactured via SLM, *J. Laser Appl.*, 2017, **29**, p 022306
12. A. Amanov, Effect of Local Treatment Temperature of Ultrasonic Nanocrystalline Surface Modification on Tribological Behavior and Corrosion Resistance of Stainless Steel 316L Produced by Selective Laser Melting, *Surf. Coat. Technol.*, 2020, **98**, p 126080
13. N.S. Al-Mamun, K.M. Deen, W. Haider, E. Asselin, and I. Shabib, Corrosion Behavior and Biocompatibility of Additively Manufactured 316L Stainless Steel in a Physiological Environment: the Effect of Citrate Ions, *Addit. Manuf.*, 2020, **34**, p 101237
14. A.B. Kale, B.K. Kim, D.I. Kim, E.G. Castle, M. Reece, and S.H. Choi, An Investigation of the Corrosion Behavior of 316L Stainless Steel Fabricated by SLM and SPS Techniques, *Mater. Charact.*, 2020, **163**, p 110204
15. M. Laleh, A.E. Hughes, S. Yang, J.L. Li, W. Xu, I. Gibson, and M.Y. Tan, Two and Three-Dimensional Characterisation of Localised Corrosion Affected by Lack-of-Fusion Pores in 316L Stainless Steel Produced by Selective Laser Melting, *Corros. Sci.*, 2020, **165**, p 108394
16. V. Cruz, Q. Chao, N. Birbilis, D. Fabijanic, P.D. Hodgson, and S. Thomas, Electrochemical Studies on the Effect of Residual Stress on the Corrosion of 316L Manufactured by Selective Laser Melting, *Corros. Sci.*, 2020, **164**, p 108314
17. C.S. Zhou, S.Y. Hu, Q.Y. Shi, H.M. Tao, Y.Y. Song, J.Y. Zheng, P. Xu, and L. Zhang, Improvement of Corrosion Resistance of SS316L Manufactured by Selective Laser Melting through Subcritical Annealing, *Corros. Sci.*, 2020, **164**, p 108353
18. M. Laleh, A.E. Hughes, W. Xu, N. Haghdad, K. Wang, P. Cizek, I. Gibson, and M.Y. Tan, On the Unusual Intergranular Corrosion Resistance of 316L Stainless Steel Additively Manufactured by Selective Laser Melting, *Corros. Sci.*, 2019, **161**, p 108189
19. M. Atapour, X. Wang, M. Persson, I.O. Wallinder, and Y.S. Hedberg, Corrosion of Binder Jetting Additively Manufactured 316L Stainless Steel of Different Surface Finish, *J. Electrochem. Soc.*, 2020, **167**, p 131503

20. V. Hauk, *Structural and Residual Stress Analysis by Nondestructive Methods*, Elsevier, Amsterdam, 1997
21. Z. Yang, B. Kan, J. Li, Y. Su, L. Qiao, and A.A. Volinsky, Pitting Initiation and Propagation of X70 Pipeline Steel Exposed to Chloride-Containing Environments, *Materials*, 2017, **10**, p 1076
22. N. Hara, K. Hirabayashi, Y. Sugawara, and I. Muto, Improvement of Pitting Corrosion Resistance of Type 316L Stainless Steel by Potentiostatic Removal of Surface MnS Inclusions, *Int. J. Corros.*, 2012, 482730
23. D. Kong, C. Dong, X. Ni, L. Zhang, H. Luo, R. Li, L. Wang, C. Man, and X. Li, The Passivity of Selective Laser Melted 316L Stainless Steel, *Appl. Surf. Sci.*, 2020, **504**, p 144495
24. X. Yue, L. Zhang, Y. Hua, J. Wang, N. Dong, X. Li, S. Xu, and A. Neville, Revealing the Superior Corrosion Protection of the Passive Film on Selective Laser Melted 316L SS in a Phosphate-Buffered Saline Solution, *Appl. Surf. Sci.*, 2020, **529**, p 147170
25. J.G. Choi and L.T. Thompson, XPS Study of As-prepared and Reduced Molybdenum Oxides, *Appl. Surf. Sci.*, 1996, **93**, p 143–149
26. P. Marcus and J.M. Grimal, The Antagonistic Roles of Chromium and Sulphur in the Passivation of Ni-Cr-Fe Alloys Studied by XPS and Radiochemical Techniques, *Corros. Sci.*, 1990, **31**, p 377–382
27. P. Keller and H.H. Strehblow, XPS Investigations of Electrochemically Formed Passive Layers on Fe/Cr-Alloys in 0.5 M H₂SO₄, *Corros. Sci.*, 2004, **46**, p 1939–1952
28. D. Kong, X. Ni, C. Dong, L. Zhang, C. Man, J. Yao, K. Xiao, and X. Li, Heat Treatment Effect on the Microstructure and Corrosion Behavior of 316L Stainless Steel Fabricated by Selective Laser Melting for Proton Exchange Membrane Fuel Cells, *Electrochim. Acta*, 2018, **276**, p 293–303
29. C. Zhou, J. Wang, S. Hu, H. Tao, B. Fang, L. Li, and Z.L. Zheng, Enhanced Corrosion Resistance of Additively Manufactured 316L Stainless Steel After Heat Treatment, *J. Electrochem. Soc.*, 2020, **167**, p 141504
30. V. Vignal, H. Krawiec, O. Heintz, and D. Mainy, Passive Properties of Lean Duplex Stainless Steels After Long-Term Ageing in Air Studied using EBSD, AES, XPS and Local Electrochemical Impedance Spectroscopy, *Corros. Sci.*, 2013, **67**, p 109–117
31. V. Vignal, H. Krawiec, and S. Le Manchet, Influence of Surface Preparation and Microstructure on the Passivity and Corrosion Behaviour of Duplex Stainless Steels, *J. Solid State Electrochem.*, 2014, **18**, p 2947–2954
32. V. Vignal, H. Zhang, O. Delrue, O. Heintz, I. Popa, and J. Peultier, Influence of Long-Term Ageing in Solution Containing Chloride Ions on the Passivity and the Corrosion Resistance of Duplex Stainless Steels, *Corros. Sci.*, 2011, **53**, p 894–903
33. N.E. Hakiki, S. Boudin, B. Rondot, and M. Da Cunha Belo, The Electronic Structure of Passive Films Formed on Stainless Steels, *Corros. Sci.*, 1995, **37**, p 1809–1822
34. H. Krawiec, V. Vignal, and J. Banas, Local Electrochemical Impedance Measurements on Inclusion-Containing Stainless Steels using Micro-capillary-Based Techniques, *Electrochim. Acta*, 2009, **54**, p 6070–6074
35. H. Krawiec, V. Vignal, O. Heintz, R. Oltra, and E. Chauveau, Dissolution of Chromium-Enriched Inclusions and Pitting Corrosion of Resulfurized Stainless Steels, *Metall. Mater. Trans. A Phys. Metall. Mater. Sci.*, 2006, **37A**, p 1541–1549
36. V. Rault, V. Vignal, H. Krawiec, and O. Tadjoua, Corrosion Behaviour of Heavily Deformed Pearlitic and Brass-Coated Pearlitic Steels in Sodium Chloride Solutions, *Corros. Sci.*, 2014, **86**, p 275–284
37. A.B. Rhouma, T. Amadou, H. Sidhom, and C. Braham, Correlation Between Microstructure and Intergranular Corrosion Behavior of Low Delta-Ferrite Content AISI 316L Aged in the Range 550–700 °C, *J. Alloys Compd.*, 2017, **708**, p 871–886

Publisher's Note Springer Nature remains neutral with regard to jurisdictional claims in published maps and institutional affiliations.